SIR Meta Distribution Analysis of a Narrow-Beam LEO Uplink

Ilari Angervuori *Student, IEEE* , Martin Haenggi *Fellow, IEEE*, and Risto Wichman

***Abstract*—We analyze a narrow-beam low earth orbit (NB LEO) terrestrial-satellite uplink from the perspective of the typical satellite base station. The user equipment (UEs) are located on the earth's surface according to a homogeneous Poisson point process (PPP). We present a simplified planar system model and focus on the point process of the approximate antenna gains of each UE in the satellite base station's antenna pattern and analyze the signal-to-interference ratio (SIR), the SIR meta distribution (MD), the signal-to-interference-plus-noise ratio (SINR) and the throughput. We present simple analytical results, some in closed form, for the performance metrics. We validate the approximate system model by comparing the results to the Monte Carlo simulated performance metrics using the more accurate system model incorporating the earth's curvature. The paper includes insightful results that help to understand the quantitative and qualitative nature of the NB LEO satellite uplink.**

***Index Terms*—Satellite uplink, low earth orbit, stochastic geometry, meta distribution, Poisson point process, throughput.**

I. Introduction

A. Motivation

Fifth-generation (5G) and beyond wireless communication systems are setting new standards of reliability and connectivity [1], [2]. The emerging Low Earth Orbit (LEO) satellite networks have the potential to significantly increase coverage, especially in far-flung areas: incorporating such networks with terrestrial networks can facilitate a seamless coverage continuum [3]. Several large LEO constellation projects have been designed and planned, including Kuiper, LeoSat, OneWeb, SpaceX and Telesat.

3GPP aims to adapt existing satellite and terrestrial networks to provide direct connectivity from hand-held equipment to LEO satellites using frequencies assigned to mobile satellite services or those assigned to legacy terrestrial networks [4]. Either way, interference from other co-channel transmitters significantly impacts the performance of LEO communication systems, especially as network density increases. We characterize the signal-to-interference ratio (SIR) at a satellite base station (SBS) using the meta distribution (MD). It allows for the *reliability* of the SBSs to be addressed by describing the percentage of successful transmissions over a period of use, given a SIR threshold. The SIR distribution can be derived from the SIR MD by averaging over the SBSs. Furthermore, we study the distributions of signal-to-interference-plus-noise ratio (SINR) and throughput.

In this paper, we balance accuracy and simplicity. We present a simplified LEO uplink model that models the user equipment transmitters (UE) on the plane, assuming a narrow antenna beam (NB) for the receiving SBS. We derive simple analytical results, including closed-form, for various performance metrics. Simple expressions provide more insight and allow us to exploit the results of well-known functions and distributions established in the literature.

B. Related work

The analysis of SIR MDs is based on stochastic geometry, which is a branch of mathematics that studies random spatial patterns. Numerous papers have applied stochastic geometry to wireless network models for terrestrial networks. Recently, stochastic geometry has also been used in satellite networks. A comprehensive literature review in [5] addresses various scenarios of fading and satellite distributions, including homogeneous point processes (p.p.).

In the case of ergodic point processes, the MD [6] of the SIR is a performance metric that gives information about the fraction of transmitters that reach a certain SIR threshold for at least a fraction of realizations of the fading gains. First introduced in [7], the analysis of SIR MDs for terrestrial networks has been well established in the literature. In [8], the SINR meta distribution was studied in urban, suburban, and rural areas with drones as aerial base stations (ABSs), but satellite communications were also addressed. The results are based on simulations and, unlike our paper, no analytical results were presented. An analytic expression for the SINR MD moments in a LEO downlink under Nakagami fading was derived in [9]. The SIR MD in a LEO downlink was also studied in [10]. To the best of our knowledge, the SIR MDs for the LEO uplink are yet to be explored.

Using the PPP for the satellite location and interferers, the throughput in a LEO uplink scenario with a fading environment that approximates Rician fading [11]. The analysis is based on a numerical inversion of the Laplace transform of the interference and is thus rather cumbersome. In [12], the satellites were modeled as a PPP on a sphere, and downlink and uplink performance were studied in a LEO backhaul link. In [13], the probability of outages was studied in a PPP constellation, and the results were compared with those of the Walker-Star and Walker-Delta constellations. Similarly to

The *Vilho, Yrjö and Kalle Väisälä Foundation* supported this work by making the research visit and fruitful collaboration with the University of Notre Dame possible.

I. Angervuori is with the Department of Electrical Engineering, Aalto University, Espoo, 02150, Finland. (email: ilari.angervuori@aalto.fi)

M. Haenggi is with the Department of Electrical Engineering, University of Notre Dame, Notre Dame, IN 46556, USA. (email: mhaenggi@nd.edu)

R. Wichman is with the Department of Electrical Engineering, Aalto University, Espoo, 02150, Finland. (email: risto.wichman@aalto.fi)

our paper, they found an optimal density that minimizes the outage probability under certain conditions. The modeling of transmitters and satellites as a p.p. was also addressed in [14]. [15] presents a LEO uplink performance analysis by modeling the transmitters as a PPP on the earth's surface. A framework for modeling the uplink performance for a massive internet-of-things-over-satellite network was presented in [16]. The optimal beamwidth and altitude for maximum coverage were studied in [17]. Using the PPP for the interferers, the terrestrial-satellite uplink interference, including interference from terrestrial base stations, is analyzed in [18] using Rayleigh fading. An expression for the mean interference from the terrestrial interferers at the satellite was derived, and the coverage was studied through the mean interference – this is not accurate in the case of NB antennas, when the variation in the interference from the main lobe is considerable, particularly for low altitudes or small densities of interferers.

The performance metrics in all the cited papers typically involve numerous integrals and infinite sums. The results are exact, but the expressions are difficult to evaluate and lack insight. In [19], analytical expressions in terms of Marcum Q-function for the LEO uplink outage probabilities were derived by modeling the interferers as the PPP in the plane and using Rician-K fading. The interference was considered solely from the satellite's side lobes, which may be unrealistic in dense networks. Furthermore, the interference side lobe component may be modeled as a constant power because of its relatively small variance. In the paper, the SIR distribution is exponential in the Rayleigh fading case when $K = 0$. In [20], it was observed that the SIR follows a gamma distribution in a Rician-K faded LEO uplink channel. With $K = 0$, the distribution is exponential. The results of our paper support the observations from both papers (namely, the distribution of SIR (30) can be tightly bounded from below with the exponential distribution for the large UE densities). In this paper, we concentrate on the interference from the main lobe by considering that the served UE is part of the homogeneous PPP of all UEs and give an exact and general characterization of the SIR distribution, which, having a heavy tail, differs significantly from the gamma distribution and is given by the Lomax distribution in the case of Rayleigh faded UEs.

C. Contribution

We present a simplified approximate system model for the NB LEO uplink and derive multiple analytical results for the SIR MD and the SIR, SINR and throughput distributions. To lubricate the analysis, we use Rayleigh fading for all transmitters. The results also describe performance metrics in the Nakagami-m and line-of-sight (LOS) fading scenarios, particularly the expected SIR, SINR and throughput, as well as the SIR and SINR tail distributions (for the SINR tail distribution, for small m). We validated the analysis by comparing it with Monte Carlo simulations with varying power fading distributions. The main contributions of this paper are as follows.

- We propose an approximate system model based on modeling the UEs on the plane and focus on the random process of approximate gains of each UE in the SBS's antenna (the *plane model*). By comparing it with Monte Carlo-simulated more accurate metrics (we also call these the *actual* performance metrics) by modeling the UEs on the surface of a spherical earth (the *spherical model*), we show that the plane model is sensible in the NB LEO.
- Using the model, we derive the moments of the SIR MD. For the first two moments, we derive closed-form expressions. By matching the first two moments, we approximate the SIR MD with the beta distribution. Furthermore, for general moments, we acquire two alternative analytical expressions. Using the first 15 moments, we find Chebyshev-Markov (CM) inequalities [21] for the SIR MD.
- From the SIR MD, we derive the SIR distribution and its mean and the variance. The latter two are infinite if there are less than $\log(2)$ UEs inside the 3 dB footprint on average. Further convergence results for the moments are also presented.
- We analyze the SINR distribution and conclude that (when the served UE belongs to the underlying PPP of all UEs), there exists a UE density that maximizes the expected SINR and the probability of coverage for a given altitude and elevation angle.
- We analyze the distribution of the network throughput and conclude that, with a large SNR (interference-limited channel), the expected normalized bit rate is given by the inverse of the mean number of UEs inside a SBS's 3 dB footprint. For small SNRs, there is an UE density that maximizes the expected throughput.

Glossary of principal symbols

Symbol	Explanation
h	Altitude of the SBSs.
ϵ	Elevation angle of the SBSs.
$G[\cdot]$	The SBS antenna gain.
φ_{RX}	Width of the SBSs 3 dB gain.
$\Theta \subset E$	Poisson p.p. on the earth's surface $E \subset \mathbb{R}^3$.
$\Phi \subset \mathbb{R}^2$	Poisson p.p. on the plane.
x_0	Nearest point to the origin in Φ.
λ	Density parameter of Φ and Θ.
κ	Parameter that reflects the approximate mean number of UEs inside a SBS's 3 dB footprint; $\kappa = h^2\pi\lambda\varphi_{\text{RX}}^2/\sin^4(\epsilon)$.
$\tilde{\kappa}$	$\kappa/\log(2)$.
g_x	Exponential (unless stated otherwise) random fading gain of a transmitter x.
θ	SIR or SINR threshold for a successful transmission.
I	Interference at the typical SBS in the plane model.
S	The signal power of the served UE at the typical SBS in the plane model.
$\mathring{I}$	Interference at the typical SBS in the spherical model.
$\mathring{S}$	The signal power of the served UE at the typical SBS in the spherical model.
$\hat{d}_{h,\epsilon}$	The distance between the SBS and the center of the footprint in the plane model.
d_0	Normalizing distance.
W	Constant noise power.
γ	Power path loss exponent.

II. System model

A. Approximate plane model of the NB LEO uplink

A terrestrial-satellite uplink Rayleigh block fading channel in a single-tier network is considered. We assume that UEs

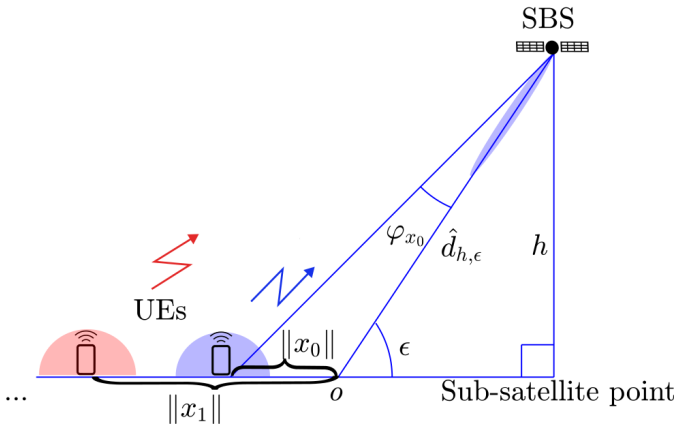

Fig. 1. The simplified NB LEO uplink system model. The SBS's antenna boresight is oriented towards o, the center of the footprint. The omnidirectionally transmitting UEs $\{x_i\}$ are distributed according to the homogeneous PPP on the plane, and each transmitter has an Euclidean norm $\|\cdot\|$. In the figure, the transmitters are projected into the line $(0,\infty)$ by their norm. The closest transmitter x_0 is the served UE.

form a homogeneous PPP $\Phi \subset \mathbb{R}^2$ of density λ. We study the SIR distribution at the typical SBS of a uniform constellation serving the terrestrial UE from which it receives the maximum mean signal power. The omnidirectionally radiating UEs can, *e.g.*, represent mobile cell phones. They are transmitting at the normalized power $P = 1$. The typical SBS is at altitude h, and its antenna's $G[\cdot]$ gain boresight is directed towards a point on the earth's surface for which the SBS is at the elevation angle ϵ. We call this the center of the footprint, which is considered the origin $o \in \mathbb{R}^2$. The values of h and ϵ together determine the distance to the satellite, which is given by the geometric relation $\hat{d}_{h,\epsilon} \triangleq h/\sin(\epsilon)$. The served UE is formally defined as

$$x_0 \triangleq \arg\min\{x \in \Phi : \|x\|\}, \tag{1}$$

where $\|\cdot\|$ is the Euclidean distance.

We write $f(x) \sim g(x)$, as $x \to a$, if the limit $\lim_{x\to a} f(x)/g(x) = 1$. For each angle φ_x between the transmitter $x \in \Phi$ and the typical SBS's antenna boresight we have

$$\varphi_x \sim D_{h,\epsilon}\|x\|, \ \|x\| \to 0, \tag{2}$$

where $D_{h,\epsilon} \triangleq \sin^2(\epsilon)/h$ is the derivative of the function $\|x\| \mapsto \varphi_x$ at $x = o$. Let us define the path loss law by

$$\ell(x) \triangleq \frac{G[\varphi_x]}{(d_x/d_0)^\gamma}, \ \ \gamma \geq 0, \tag{3}$$

where d_0 is a normalizing distance. Combining (2) with (3),

$$\ell(x) \sim \frac{G[D_{h,\epsilon}\|x\|]}{(d_x/d_0)^\gamma}, \ \ \|x\| \to 0. \tag{4}$$

Furthermore, we assume a NB and the relevant transmitters are located in a small region close to each other around o and $d_x \approx \hat{d}_{h,\epsilon}$ for the relevant $x \in \Phi$. Along these lines, the random process of path losses $\{x \in \Phi : \ell(x)\}$ is approximated with the gain process (GP)

$$\mathcal{G} = \{x \in \Phi : G[D_{h,\epsilon}\|x\|]\} \tag{5}$$

multiplied by the constant $(d_0/\hat{d}_{h,\epsilon})^\gamma$. In the system model, the p.p. of the spatial locations of the UEs and the corresponding path losses is approximated by the one-dimensional GP reflecting the approximate UEs signal gains at the typical SBS's antenna.

In addition, for each UE $x \in \Phi$, the transmit power is multiplied by an independent exponentially distributed random fading gain g_x of mean 1 adding another random layer in the received signal strength.

In this work, we focus on LEO altitudes of $h \in [200, 2000]$ km. The antenna gain $G[\cdot] : [0,\infty) \to (0,1]$ is assumed to be Gaussian, *i.e.*,

$$G[\varphi] = 2^{-\varphi^2/\varphi^2_{\text{RX}}}, \tag{6}$$

where φ_{RX} is the width of the 3 dB antenna gain. Throughout this paper, we will use the value $\varphi_{\text{RX}} = 1.6°$, which corresponds to the LEO antenna pattern proposed in the International Telecommunication Union Recommendations (ITU-R) [22]. Furthermore, we will consider that the SBS is at least at the elevation angle 45° w.r.t. the satellite (with an exception in Figures 2a, 2b and 3).

B. The plane model as an approximation of the spherical model

The system model presented in II-A approximates the spherical model where the UEs are located on the earth's surface. We denote the homogeneous PPP of density λ on the earth's surface by $\Theta \subset E$. We define $\mathring{x}_0 \triangleq \arg\min\{x \in \Theta : d_x\}$, and $o_E \in E$ is the center of the footprint on E. The angles $\{\varphi_x\}$ and the distances $\{d_x\}$, and consequently the path losses $\{\ell(x)\}$, are accurate for $x \in \Theta$ in the spherical model.

The total total power received from the UEs in Θ is defined as

$$\mathring{P}_{\text{tot}} \triangleq \mathring{I} + \mathring{S} = \sum_{x\in\Theta} g_x \ell(x) = \sum_{x\in\Theta} \frac{g_x G[\varphi_x]}{(d_x/d_0)^\gamma}, \tag{7}$$

where $\mathring{S}$ is the signal strength at the receiver of $\mathring{x}_0$, and $\mathring{I}$ is the interference component consisting of the received signal powers from $\Theta \setminus \{\mathring{x}_0\}$. We call $\mathring{P}_{\text{tot}}$ the actual total received power. For the distance between the SBS and o_E, we have

$$d_{h,\epsilon} \triangleq d_{o_E} = \sqrt{R_\oplus^2 + (R_\oplus + h)^2 - 2R_\oplus(R_\oplus + h)\cos(\xi)}, \tag{8}$$

where $R_\oplus = 6378$ km is the earth's mean radius, and $\xi = \xi(\epsilon)$ is the central angle between o_E and the sub-satellite point (the details are given in Appendix A). The difference between $\hat{d}_{h,\epsilon}$ and $d_{h,\epsilon}$ and the approximation (2) of the angle φ_x causes an error in the received total power. The error increases for smaller ϵ. For $\epsilon = \pi/2$, when $\xi = 0$, $d_{h,\epsilon} = h = \hat{d}_{h,\epsilon}$ – furthermore, (2) holds also in the spherical model. As will be seen, the error does not noticeably affect the received total power for $\gamma = 2$.

We validate the approximate system model by studying the convergence properties of the mean and the second moment of the simulated $\mathring{P}_{\text{tot}}$ to the theoretical mean and the second moment of

$$P_{\text{tot}} \triangleq \frac{1}{(\hat{d}_{h,\epsilon}/d_0)^\gamma} \sum_{x\in\Phi} g_x G[D_{h,\epsilon}\|x\|]. \tag{9}$$

The fading models are equal in the plane and spherical models, and the difference is in the geometry. Hence, we focus on the geometric accuracy of the approximate model and set $g_x \equiv 1$ in this subsection. The fading does not affect the first moment of the received total power. For $g_x \equiv 1$, [23, Cor. 4.8] gives the expected value and the variance of P_{tot}

$$\begin{aligned}\mathbb{E}(P_{\text{tot}}) &= \left(\frac{d_0}{\hat{d}_{h,\epsilon}}\right)^{\gamma} \int_{\mathbb{R}^2} G[D_{h,\epsilon}\|x\|]\lambda dx \\ &= \left(\frac{d_0}{\hat{d}_{h,\epsilon}}\right)^{\gamma} \int_0^1 r\lambda_{\mathcal{G}}(r)dr = \frac{d_0^{\gamma} h^{2-\gamma}\pi\lambda\varphi_{\text{RX}}^2}{\sin^{4-\gamma}(\epsilon)\log(2)},\end{aligned} \tag{10}$$

$$\begin{aligned}\text{var}(P_{\text{tot}}) &= \mathbb{E}(P_{\text{tot}}^2) - \mathbb{E}(P_{\text{tot}})^2 \\ &= \left(\frac{d_0}{\hat{d}_{h,\epsilon}}\right)^{2\gamma} \int_{\mathbb{R}^2} G[D_{h,\epsilon}\|x\|]^2\lambda dx \\ &= \left(\frac{d_0}{\hat{d}_{h,\epsilon}}\right)^{2\gamma} \int_0^1 r^2\lambda_{\mathcal{G}}(r)dr = \frac{d_0^{\gamma}\sin^{\gamma}(\epsilon)}{2h^{\gamma}}\mathbb{E}(P_{\text{tot}}),\end{aligned} \tag{11}$$

respectively. The density $\lambda_{\mathcal{G}}(r) = \tilde{\kappa}/r$ and the Poisson property of the GP (which is needed for the variance) follow from Corollary 1.

An immediate observation from (10) and (11) is that for the free-space path loss exponent $\gamma = 2$, for given λ, ϵ and φ_{RX}, the mean of the total received power does not depend on the altitude of the typical SBS; the path loss becomes increasingly prominent, but there are more UEs present in the main lobe as we increase h. Furthermore, $\text{var}(P_{\text{tot}})$ rapidly increases when we decrease the altitude. On the other hand, P_{tot} approaches a constant for large h. For $\gamma > 2$, the expected total received power decreases as the altitude increases and vice versa. For $\gamma = 4$, $\mathbb{E}(P_{\text{tot}})$ does not depend on the elevation angle of the SBS.

Figures 2a and 2b show the total received powers $\mathring{P}_{\text{tot}}$ and P_{tot} for $\gamma \in \{2, 4\}$ for multiples ϵ and h. One can see that the insights of the theoretical model apply to the spherical model, especially for $\gamma = 2$.

Figure 3 shows the ratio of the second moments $\mathbb{E}(\mathring{P}_{\text{tot}}^2)/\mathbb{E}(P_{\text{tot}}^2)$ w.r.t. φ_{RX} for different values of h and γ. The density $\lambda = 1/\text{km}^2$ and the elevation angle $\epsilon = 35°$, which is the minimum elevation angle in a LEO system proposed in [24]. Due to the geometry, it is the worst-case scenario for the error between the models. The ratios for $\epsilon > 35°$ are closer to 1 for each h. The ratios tend to 1 for $\gamma = 2$ as $\varphi_{\text{RX}} \to 0$. There is a threshold after which $\mathbb{E}(\mathring{P}_{\text{tot}}^2)$ becomes exponentially larger than $\mathbb{E}(P_{\text{tot}}^2)$. The differences in the geometry cause this. However, the horizon restricting the energy from the UEs in the spherical model limits this exponential increase for larger φ_{RX}. For $\gamma = 4$, convergence to 1 does not happen: this is due to the difference in the average of $\{d_x\}_{x\in\Theta}$ and $\{d_x\}_{x\in\Phi}$, which gets canceled for $\gamma = 2$. The theoretical model could be improved using the more complicated $d_{h,\epsilon}$ instead of $\hat{d}_{h,\epsilon}$ in (9). However, the theoretical SIR (13) is independent of the path loss exponent, which also holds (up to the precision we are interested in) in the spherical model. We will validate this using both path loss exponents in the Sections III and IV simulations.

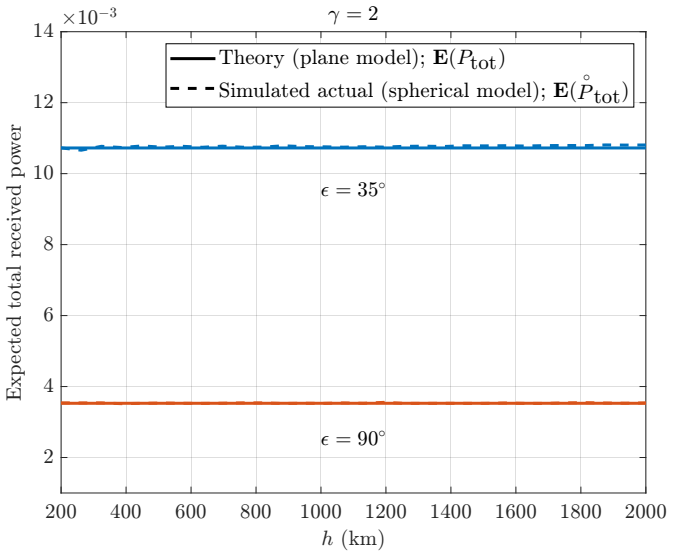

(a) For the path loss exponent $\gamma = 2$, the total received power is approximately independent of the altitude

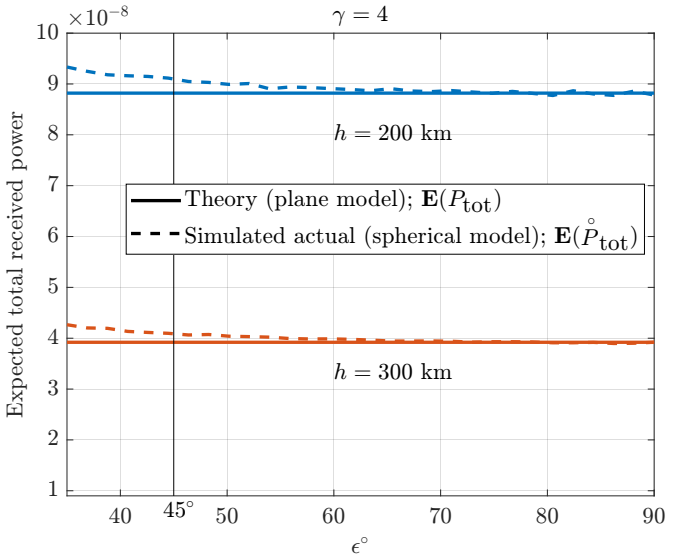

(b) For $\gamma = 4$, the total received power is approximately independent of the elevation angle

Fig. 2. The expected total received power. The theory and the actual simulated values are compared. The parameters $\varphi_{\text{RX}} = 1.6°, P = 1, \lambda = 1/\text{km}^2, \gamma \in \{2, 4\}, h \in [200, 2000]$ km, $\epsilon \in (35, 90)°$ are used.

Similar but faster convergence to 1 was observed for the first moments $\mathbb{E}(\mathring{P}_{\text{tot}})/\mathbb{E}(P_{\text{tot}})$ than for $\mathbb{E}(\mathring{P}_{\text{tot}}^2)/\mathbb{E}(P_{\text{tot}}^2)$.

Based on these observations, we put forth that, for $\gamma = 2$ or $\epsilon = \pi/2$;

$$\begin{aligned}&\mathbb{E}(P_{\text{tot}}) \sim \mathbb{E}(\mathring{P}_{\text{tot}}), \\ &\mathbb{E}(P_{\text{tot}}^2) \sim \mathbb{E}(\mathring{P}_{\text{tot}}^2), \quad \varphi_{\text{RX}} \to 0.\end{aligned} \tag{12}$$

Furthermore, it is natural to conjecture that the convergence holds for any moment and thus for the distribution. Throughout this paper, we will validate the simplified system model by

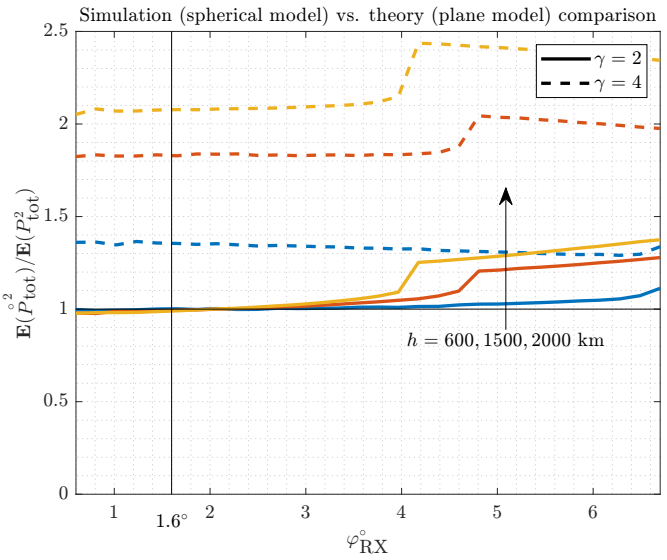

Fig. 3. The ratio of the second moments of the simulated and theoretical total received powers. The parameters $h \in \{600, 1500, 2000\}$ km, $\lambda = 1/\text{km}^2$, $\epsilon = 35°$, $\varphi_{\text{RX}} \in [0.6°, 6.7°]$ and $\gamma \in \{2, 4\}$ are used.

quantitatively comparing the theoretical and the actual SIR, the SINR, the throughput distributions and the SIR MDs.

III. The Signal-to-Interference Ratio and Its Meta Distribution

A. The definition of the SIR MD

We begin by defining the signal-to-interference ratio at the typical SBS:

$$\text{SIR} \triangleq \frac{S}{I} = \frac{Pg_{x_0}G[D_{h,\epsilon}\|x_0\|]/(\hat{d}_{h,\epsilon}/d_0)^\gamma}{\sum\limits_{x\in\Phi\setminus\{x_0\}} Pg_xG[D_{h,\epsilon}\|x\|]/(\hat{d}_{h,\epsilon}/d_0)^\gamma} = \frac{g_{x_0}G[D_{h,\epsilon}\|x_0\|]}{\sum\limits_{x\in\Phi\setminus\{x_0\}} g_xG[D_{h,\epsilon}\|x\|]}. \tag{13}$$

The terms $(\hat{d}_{h,\epsilon}/d_0)^\gamma$ cancel each other out, and the path loss exponent does not affect the SIR. This property follows from the simplified system model of the NB LEO. However, this also holds for the actual performance metrics using the spherical model, namely for $\mathring{\text{SIR}} \triangleq \mathring{S}/\mathring{I}$; this is a substantial difference from the usual terrestrial models, where the SIR depends strongly on the path loss exponent.

The SIR MD is the distribution of the random variable

$$\mathcal{P}(\theta) \triangleq \mathbb{P}(\text{SIR} > \theta|\Phi). \tag{14}$$

The probability $\mathcal{P}(\theta)$ is interpreted as the fraction of time that the SIR exceeds θ at the typical SBS when the fading varies. Furthermore, because Φ is ergodic, the fractions can be interpreted to be taken over all spatial locations on the plane, given a realization of Φ. In this sense, the SIR MD describes the reliability of the typical SBS in a uniform constellation of SBSs.

B. Relative gain process

Definition 1 (Relative gain process (RGP))**.** The relative gain process is defined as

$$\mathcal{G} \triangleq \left\{ x \in \Phi \setminus \{x_0\} : \frac{G[D_{h,\epsilon}\|x\|]}{G[D_{h,\epsilon}\|x_0\|]} \right\}, \tag{15}$$

where x_0 is the closest transmitter to the origin, *i.e.*, the served UE (1).

Lemma 1. The RGP is a PPP on $(0, 1) \ni r$ with the density function

$$\lambda_{\mathcal{G}}(r) = \tilde{\kappa}/r, \tag{16}$$

where $\tilde{\kappa} = \kappa/\log(2)$ and

$$\kappa \triangleq \frac{h^2\pi\lambda\varphi_{\text{RX}}^2}{\sin^4(\epsilon)} \tag{17}$$

is approximately the mean number of UEs inside any SBS's 3 dB footprint. The interpretation of κ is exact in the limit $\varphi_{\text{RX}} \to 0$ and is tighter for large ϵ, given λ, h and φ_{RX}.

Proof. Given in Appendix B. □

For any measurable function $v(\cdot) : \mathbb{R}^d \to [0, 1]$ such that $\int_{\mathbb{R}^d} |\log v(x)|\lambda_\Psi(x)dx < \infty$, the probability generating functional (PGFL) $\mathfrak{G}(\cdot)$ of a p.p. Ψ is defined by

$$\mathfrak{G}_\Psi[v] \triangleq \mathbb{E}\prod_{x\in\Psi} v(x). \tag{18}$$

We use Lemma 1 to derive the PGFL of the RGP [25, Eq. 3.30]

$$\mathfrak{G}_{\mathcal{G}}[v] = \exp\left\{-\int_{\mathbb{R}}(1 - v(r))\lambda_{\mathcal{G}}(r)dr\right\} = \exp\left\{-\tilde{\kappa}\int_0^1 (1 - v(r))/rdr\right\}. \tag{19}$$

Corollary 1 (GP = RGP)**.** *$\mathcal{G}$ is independent of the distribution of x_0. Furthermore, the GP is equivalent to the RGP.*

Proof. One can see from the reasoning given in Appendix B that the conditioned p.p. $(\mathcal{G}|(\|x_0\| = r))$ is equivalent to $\mathcal{G}$ for any $r \in [0, \infty)$. In particular, we may condition $x_0 = o$, and by Slivnyak's theorem, we retrieve the GP (5). □

C. Moments of the SIR MD

Proposition 1 (Moments of the SIR MD)**.** *The first and the second moments of the SIR MD in a NB LEO uplink when all transmitters experience Rayleigh fading, are given by*

$$M_1(\theta) = (1 + \theta)^{-\tilde{\kappa}}, \tag{20}$$

$$M_2(\theta) = e^{-\tilde{\kappa}\theta/(1+\theta)}(1 + \theta)^{-\tilde{\kappa}}, \tag{21}$$

respectively. The general moments $b \in \mathbb{C}$ are given by

$$M_b(\theta) = \exp\left\{-\theta b\tilde{\kappa}\,{}_3F_2(1, 1, 1 + b; 2, 2; -\theta)\right\}, \tag{22}$$

where ${}_3F_2(\cdot)$ is the hypergeometric function. Furthermore, for $b \in \mathbb{N}$,

$$M_b(\theta) = \exp\left\{\frac{\tilde{\kappa}}{(b-1)!}\sum_{k=1}^{b}\begin{bmatrix} b \\ k \end{bmatrix}\text{Li}_{2-k}(-\theta)\right\}, \tag{23}$$

where $\left[{n \atop k}\right]$ *is the first kind's unsigned Stirling number, and* $\mathrm{Li}_{2-k}(\cdot)$ *is the polylogarithm.*

Proof. Given in Appendix E. □

Remark 1. The *hypergeometric series* representation

$$ {}_3F_2(1,1,1+b;2,2;-\theta) = \sum_{n=0}^{\infty} \frac{(1)_n (1)_n (1+b)_n}{(2)_n (2)_n} \frac{(-\theta)^n}{n!}, \tag{24} $$

where $(a)_n \triangleq a(a+1)\cdots(a+n-1)$ is the rising Pochhammer factorial, is divergent for $\theta > 1$. Hence, the expression (22) is the analytic continuation of the hypergeometric series (*i.e.*, the hypergeometric function). Equation (23) may be advantageous because the polylogarithm has better software support than the generalized hypergeometric function. Alternatively, $M_b(\theta)$ may be evaluated by integrating the exponent in (58) numerically.

We denote the random variable SIR = SIR_κ to emphasize that the properties of the SIR are solely determined by κ. We denote the SIR MD by

$$ F_{\text{SIR MD}}^{[\kappa,\theta]}(y) \triangleq \mathbb{P}(\mathbb{P}(\mathrm{SIR}_\kappa > \theta|\Phi) > y). \tag{25} $$

In words, $F_{\text{SIR MD}}^{[\kappa,\theta]}(y)$ gives the fraction of SBSs that reach the reliability y.

D. Chebyshev-Markov inequalities

Given a moment sequence $(M_k)_{k=0}^n$, the order n CM inequalities give the pointwise infimum and supremum

$$ \inf_{F\in\mathcal{F}_n} F(y), \quad \sup_{F\in\mathcal{F}_n} F(y) \tag{26} $$

for any $y \in [0,1]$, where $\mathcal{F}_n$ is the set of the distributions that agree with the moment sequence. The inequalities established by the infima and suprema are called the CM inequalities [21, Thm. 1]. We use the CM inequalities to validate the theory by comparing the CM inequalities derived from the moments (23) to the simulated SIR MD in the spherical model.

E. Approximation of the SIR MD

In many cases, the beta distribution effectively approximates the SIR MD [7], [26], [27]. If α and β are the shape parameters of the beta distribution, the first and the second moments are given by $\alpha/(\alpha+\beta)$ and $\alpha(\alpha+1)/((\alpha+\beta)(\alpha+\beta+1))$, respectively. Using the expressions (20) and (21) for the first two moments and matching them to the corresponding moments of the beta distribution, we can solve for α and β:

Proposition 2 (Approximation of the SIR MD with the beta distribution)**.** *The parameters* α *and* β *for the beta distribution are given as*

$$ \begin{aligned} \alpha &= \left(\frac{M_1(\theta)(1-M_1(\theta))}{M_2(\theta)-M_1(\theta)^2} - 1\right) M_1(\theta) \\ &= \frac{e^{\tilde{\kappa}\theta/(1+\theta)} - 1}{(1+\theta)^{\tilde{\kappa}} - e^{\tilde{\kappa}\theta/(1+\theta)}}, \end{aligned} \tag{27} $$

$$ \begin{aligned} \beta &= \left(\frac{M_1(\theta)(1-M_1(\theta))}{M_2(\theta)-M_1(\theta)^2} - 1\right) (1-M_1(\theta)) \\ &= \alpha(1+\theta)^{\tilde{\kappa}} - \alpha. \end{aligned} \tag{28} $$

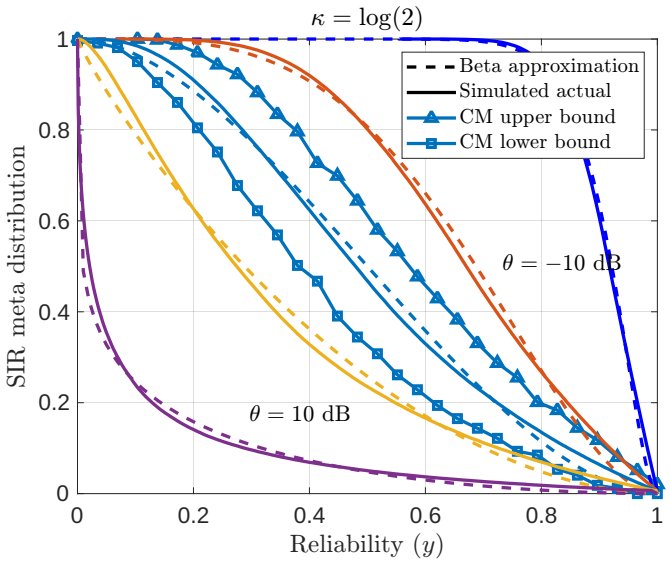

Fig. 4. The simulated actual SIR MD and the corresponding beta distribution for $\theta \in \{-10, -3, 0, 3, 10\}$ dB (from top to bottom). The parameters $\gamma = 2$, $\lambda = 7 \cdot 10^{-5}/\mathrm{km}^2$, $h = 2000$ km, $\epsilon = 90°$ and $\varphi_{\mathrm{RX}} = 1.6°$ were used that correspond to $\kappa = \log(2)$. Order 15 CM inequalities are depicted for $\theta = 0$ dB.

The SIR MD can be approximated by the beta distribution:

$$ F_{\text{SIR MD}}^{[\kappa,\theta]}(y) \approx \begin{cases} 1 - I_y(\alpha,\beta), & y \in [0,1] \\ 1, & y < 0 \\ 0, & y > 1, \end{cases} \tag{29} $$

where $I.(\alpha,\beta)$ *is the regularized incomplete beta function.*

In Figures $4-6$, we compare the simulated actual SIR MD $\mathbb{P}(\mathbb{P}(\mathring{\mathrm{SIR}} > \theta|\Theta) > y)$ to the beta distribution approximation (29) for various κ and θ. Order 15 CM inequalities are drawn for $\theta \in \{0, -3, -13\}$ to the respective figures. Other inequalities are omitted to avoid cluttering the figures. For the simulations, we use different values of ϵ, γ and h. The density λ is scaled accordingly to meet the given κ. In particular, in Figure 6, one can see that for the low elevation angles, the plane model is less accurate than for large elevation angles – this is due to the spherical shape of the earth that becomes increasingly prevalent in the spherical model, but also because κ does not correspond accurately to the actual mean number of UEs inside the 3 dB footprint.

IV. SIR, SINR AND THROUGHPUT DISTRIBUTIONS

A. SIR distribution

The SIR distribution is easy to obtain from the SIR MD since the first moment $M_1(\cdot)$ is just the complementary cumulative distribution function (CCDF) $F_{\mathrm{SIR}}^{[\kappa]}(\cdot)$ of SIR. We have

$$ \begin{aligned} F_{\mathrm{SIR}}^{[\kappa]}(\theta) &\triangleq \mathbb{P}(\mathrm{SIR}_\kappa > \theta) = \mathbb{E}_\Phi \mathbb{P}(\mathrm{SIR}_\kappa > \theta|\Phi) = M_1(\theta) \\ &= (1+\theta)^{-\tilde{\kappa}}. \end{aligned} \tag{30} $$

If θ is the SIR threshold needed for a successful transmission, (30) is called the *transmission success probability*.

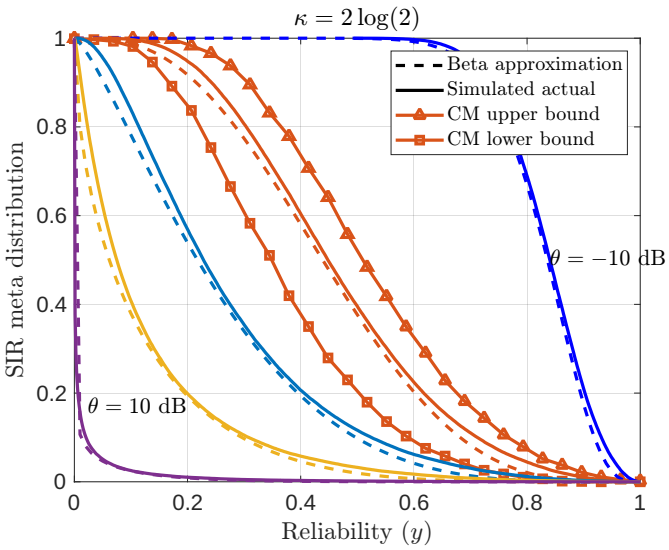

Fig. 5. The simulated actual SIR MD and the corresponding beta distribution for $\theta \in \{-10, -3, 0, 3, 10\}$ dB (from top to bottom). The parameters $\gamma = 4$, $\lambda = \lambda = 3.7 \cdot 10^{-4}/\text{km}^2$, $h = 1200$ km, $\epsilon = 80°$ and $\varphi_{\text{RX}} = 1.6°$ were used that correspond to $\kappa = 2\log(2)$. Order 15 CM inequalities are depicted for $\theta = -3$ dB.

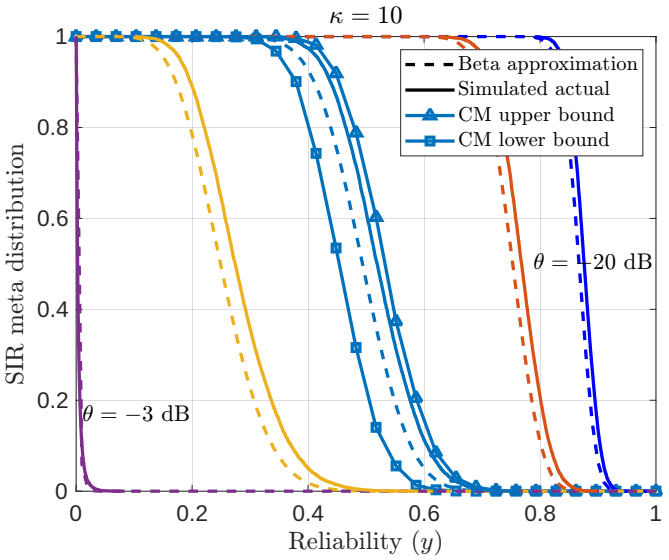

Fig. 6. The simulated actual SIR MD and the corresponding beta distribution for $\theta \in \{-20, -17, -13, -10, -3\}$ dB (from top to bottom). The parameters $\gamma = 2$, $\lambda = 3 \cdot 10^{-3}/\text{km}^2$, $h = 200$ km, $\epsilon = 60°$ and $\varphi_{\text{RX}} = 1.6°$ were used that correspond to $\kappa = 10$. Order 15 CM inequalities are depicted for $\theta = -13$ dB.

The mean and the variance of the SIR are given by

$$\mathbb{E}(\text{SIR}_\kappa) = \int_0^\infty F_{\text{SIR}}^{[\kappa]}(y)dy = \frac{1}{\tilde{\kappa} - 1}, \ \tilde{\kappa} > 1, \tag{31}$$

$$\begin{aligned}\text{var}(\text{SIR}_\kappa) &= 2\int_0^\infty y F_{\text{SIR}}^{[\kappa]}(y)dy - \left(\int_0^\infty F_{\text{SIR}}^{[\kappa]}(y)dy\right)^2 \\ &= \frac{\tilde{\kappa}}{(\tilde{\kappa} - 2)(\tilde{\kappa} - 1)^2}, \ \tilde{\kappa} > 2,\end{aligned} \tag{32}$$

respectively. The mean and variance are divergent for $\tilde{\kappa} \leq 1$, that is, $\kappa \leq \log(2)$: Having fewer than $\log(2)$ UEs inside the 3 dB footprint on average, a large fraction of SBSs have a very high SIR, and, on the other hand, a significant fraction has a low SIR, and consequently, the expected SIR and its variance are infinite. Under this threshold, the channel is essentially noise-limited. In the regime $\log(2) < \kappa \leq 2\log(2)$, the SIR converges in mean but exhibits unbounded variance.

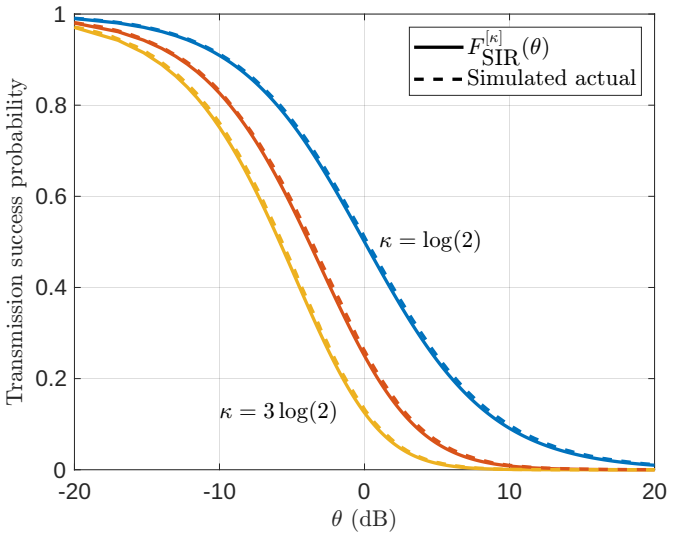

Fig. 7. The simulated actual SIR distribution and the corresponding theoretical distribution for $\kappa \in \{\log(2), 2\log(2), 3\log(2)\}$ dB (from top to bottom). The parameters $\gamma = 4$, $h = 600$ km, $\epsilon = 80°$, $\varphi_{\text{RX}} = 1.6°$ and $\lambda \in \{7.4 \cdot 10^{-4}, 1.5 \cdot 10^{-3}, 2.2 \cdot 10^{-3}\}/\text{km}^2$ were used to match the respective κ.

The decay rate of a random variable Y is defined as $\rho(y) \triangleq -\log(\mathbb{P}(Y > y))/y$ [28, Eq. 66]. The asymptotic decay rate for the SIR is given by

$$\begin{aligned}\rho \triangleq \lim_{y\to\infty} \rho(y) &= \lim_{y\to\infty} -\frac{F_{\text{SIR}}^{[\kappa]}(y)}{y} \\ &= \lim_{y\to\infty} -\frac{\log((1+y)^{-\tilde{\kappa}})}{y} = 0.\end{aligned} \tag{33}$$

The SIR distribution has, in fact, a slowly decaying tail for any κ. The condition (33) is equivalent to the distribution being heavy-tailed in the sense that the exponential moment $\mathbb{E}(e^{t\text{SIR}_\kappa})$ is divergent for any $t > 0$ [29, Thm. 2.6]. It is worth noting that (30) is Burr distribution, *i.e.*, Pareto Type II (Lomax) distribution. Its nth moment exists if and only if $\tilde{\kappa} > n$.

In Figure 7, we plot the theoretical SIR distribution and the actual simulated success probability $\mathbb{P}(\text{SIR} > \theta)$ for various κ.

B. SINR distribution

The tail behavior observed in the model is due to the lack of sidelobes or noise. In this section, we add a constant (normalized scalar) noise power term $W > 0$ to I and analyze the SINR.

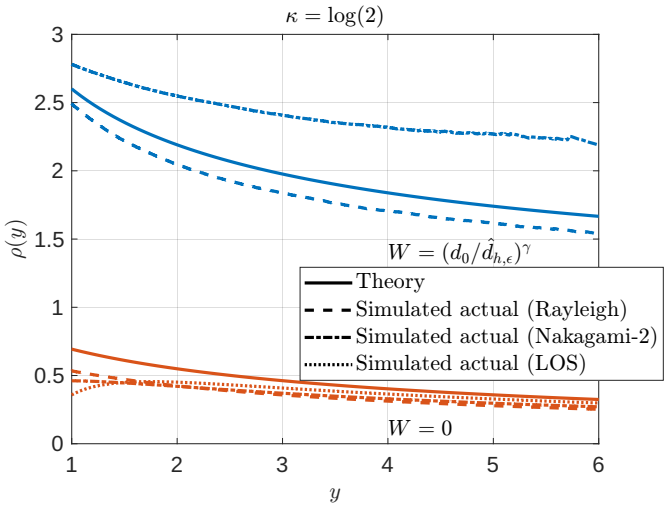

Fig. 8. The decay rates of $F_{\text{SIR}}^{[\kappa]}(y)$ and $F_{\text{SINR}}^{[\kappa,W]}(y)$ and the corresponding simulated decay rates in the spherical model. We use the parameters $\gamma = 2$, $W = (d_0/\hat{d}_{h,\epsilon})^\gamma$ (for the SINR), $\epsilon = 45°, \varphi_{\text{RX}} = 1.6°$ and $h = 700$ km. The density $\lambda = 1.4 \cdot 10^{-4}/\text{km}^2$ was used to match $\kappa = \log(2)$.

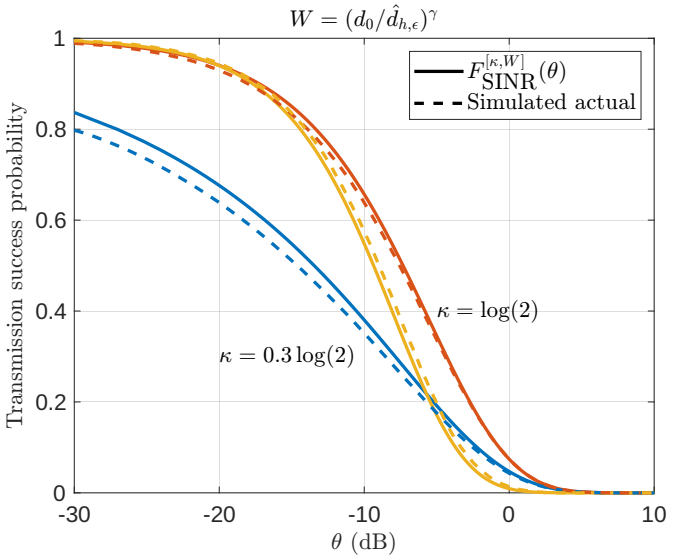

Fig. 9. The simulated actual SINR distribution and the corresponding theoretical distribution for $\kappa \in \{\log(2), 5\log(2), 0.3\log(2)\}$ dB (from top to bottom). The parameters $\gamma = 2$, $h = 200$ km, $\epsilon = 50°$, $\varphi_{\text{RX}} = 1.6°$, $W = (d_0/\hat{d}_{h,\epsilon})^\gamma$ and $\lambda \in \{2.4 \cdot 10^{-3}, 1.2 \cdot 10^{-2}, 7.3 \cdot 10^{-4}\}/\text{km}^2$ were used to match the respective κ.

Proposition 3 (SINR distribution)**.** *The transmission success probability is given by*

$$F_{\text{SINR}}^{[\kappa,W]}(\theta) \triangleq \mathbb{P}(\text{SINR}_{\kappa,W} > \theta) = \mathbb{P}\left(\frac{S}{I+W} > \theta\right)$$
$$= \mathbb{P}\left(g_{x_0} > \sum_{x\in\Phi\setminus\{x_0\}} \frac{G[D_{h,\epsilon}\|x\|]\theta}{G[D_{h,\epsilon}\|x_0\|]} g_x + \frac{W(\hat{d}_{h,\epsilon}/d_0)^\gamma\theta}{G[D_{h,\epsilon}\|x_0\|]}\right)$$
$$\overset{(a)}{=} \mathbb{E}_\Phi \mathbb{E}_g \exp\left\{-\theta \sum_{x\in\Phi} G[D_{h,\epsilon}\|x\|] g_x\right\} \cdot$$
$$\mathbb{E}_\Phi \exp\left\{-W(\hat{d}_{h,\epsilon}/d_0)^\gamma\theta / G[D_{h,\epsilon}\|x_0\|]\right\}$$
$$\overset{(b)}{=} \mathbb{E} \prod_{x\in\Phi} \frac{1}{1+\theta G[D_{h,\epsilon}\|x\|]} E_{\tilde{\kappa}+1}\left(W(\hat{d}_{h,\epsilon}/d_0)^\gamma\theta\right) \tilde{\kappa}$$
$$= \tilde{\kappa}(1+\theta)^{-\tilde{\kappa}} E_{\tilde{\kappa}+1}\left(W(\hat{d}_{h,\epsilon}/d_0)^\gamma\theta\right), \tag{34}$$

where $E_{\tilde{\kappa}+1}(\cdot)$ is the generalized exponential integral.

Proof. In (a), we used Corollary 1. In (b) we used the Laplace transform of the inverse largest gain (52). □

One can derive the asymptotic decay rate

$$\rho = -\lim_{y\to\infty} \frac{\log\left(F_{\text{SINR}}^{[\kappa,W]}(y)\right)}{y} = W(\hat{d}_{h,\epsilon}/d_0)^\gamma. \tag{35}$$

The mean and the variance

$$\mathbb{E}(\text{SINR}_{\kappa,W}) = \int_0^\infty F_{\text{SINR}}^{[\kappa,W]}(y)dy,$$
$$= \tilde{\kappa}\int_0^\infty (1+y)^{-\tilde{\kappa}} E_{\tilde{\kappa}+1}\left(W(\hat{d}_{h,\epsilon}/d_0)^\gamma y\right) dy, \tag{36}$$
$$\text{var}(\text{SINR}_{\kappa,W})$$
$$= 2\int_0^\infty y F_{\text{SINR}}^{[\kappa,W]}(y)dy - \left(\int_0^\infty F_{\text{SINR}}^{[\kappa,W]}(y)dy\right)^2 \tag{37}$$

are difficult to evaluate other than numerically. Asymptotically (the proof is given in Appendix D),

$$\mathbb{E}(\text{SINR}_{\kappa,W}) \sim 1/(\tilde{\kappa}-1), \text{ as } \kappa\to\infty. \tag{38}$$

1) Upper bound of the SINR: We may derive an upper bound for the expected SINR by solving the expected value of the $\text{SINR}_{\kappa,W}$ with the condition $I = 0$, *i.e.*, $\text{SNR}_{\kappa,W}$.

$$\mathbb{E}(\text{SINR}_{\kappa,W}) \le \mathbb{E}(\text{SNR}_{\kappa,W}) = \int_0^\infty \mathbb{P}(S/W > y)dy$$
$$= \tilde{\kappa}\int_0^\infty E_{\tilde{\kappa}+1}\left(W(\hat{d}_{h,\epsilon}/d_0)^\gamma y\right) dy$$
$$= \tilde{\kappa}\int_0^\infty -E_{\tilde{\kappa}+2}\left(W(\hat{d}_{h,\epsilon}/d_0)^\gamma y\right)$$
$$= \frac{\tilde{\kappa}}{W(\hat{d}_{h,\epsilon}/d_0)^\gamma(\tilde{\kappa}+1)}. \tag{39}$$

The term W suppresses the tails, and consequently, $\mathbb{E}(\text{SINR}_{\kappa,W})$ is finite for all $\kappa \ge 0$.

The function $\kappa \mapsto \mathbb{E}(\text{SNR}_{\kappa,W})$ is monotonically increasing, and we have

$$\lim_{\kappa\to 0} \mathbb{E}(\text{SNR}_{\kappa,W}) = 0, \tag{40}$$

and

$$\lim_{\kappa\to\infty} \mathbb{E}(\text{SNR}_{\kappa,W}) = \frac{d_0^\gamma}{\hat{d}_{h,\epsilon}^\gamma W}. \tag{41}$$

This is not surprising because x_0 is likely close to o for high densities; in the limit $\kappa \to \infty$, the randomness is solely in the fading, resulting in the exponential variable of rate $(\hat{d}_{h,\epsilon}/d_0)^\gamma W$.

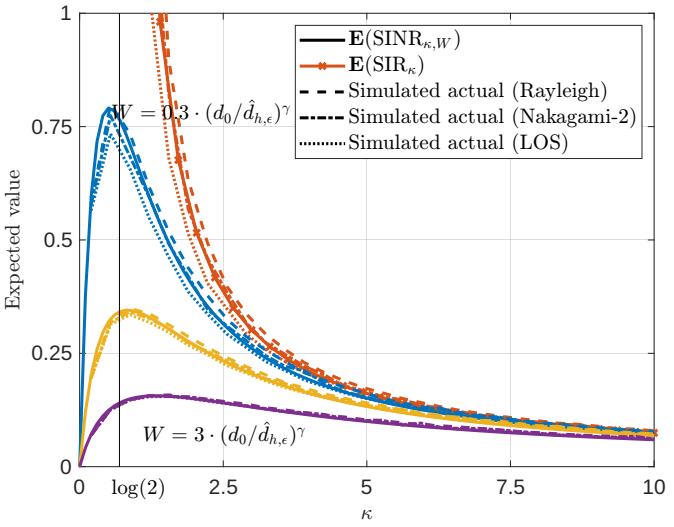

Fig. 10. The simulated actual expected SINR and SIR with the theoretical values for $W \in \{0.3, 1, 3\} \cdot (d_0/\hat{d}_{h,\epsilon})^{\gamma}$ (from top to bottom) and $\kappa \in [0, 10]$. The parameters $\gamma = 4$, $h = 1500$ km, $\epsilon = 80°$, $\varphi_{\mathrm{RX}} = 1.6°$ and $\lambda \in [0, 1.7 \cdot 10^{-3}]/\mathrm{km}^2$ were used to match the respective κ.

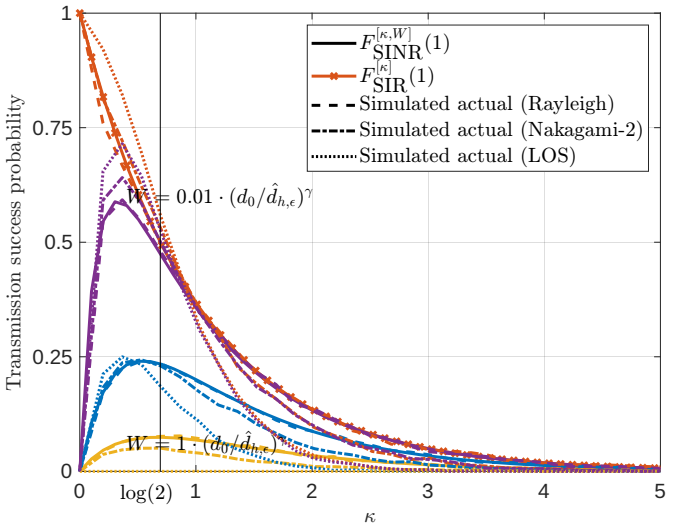

Fig. 11. The simulated actual coverage probabilities and the theoretical values with $\theta = 1$ for $W \in \{0.01, 0.3, 1\} \cdot (d_0/\hat{d}_{h,\epsilon})^{\gamma}$ (from top to bottom) and for $\kappa \in [0, 5]$. The parameters $\gamma = 2$, $h = 1500$ km, $\epsilon = 90°$, $\varphi_{\mathrm{RX}} = 1.6°$ and $\lambda \in [0, 9.1 \cdot 10^{-4}]/\mathrm{km}^2$ were used to match the respective κ.

Because $\mathbb{E}(\mathrm{SINR}_{\kappa,W}) \leq \mathbb{E}(\mathrm{SIR}_{\kappa})$, the expectation of the SINR has to go to 0 in the limit $\kappa \to \infty$. By the mean value theorem, there exists a maximum $0 < \kappa_E^{[W]} \triangleq \arg\max\{\kappa : \mathbb{E}(\mathrm{SINR}_{\kappa,W})\} < \infty$. Similarly, a maximizing κ for the coverage probability $\kappa_P^{[W,\theta]} \triangleq \arg\max\{\kappa : F^{[\kappa,W]}_{\mathrm{SINR}}(\theta)\}$ exists for any given θ and $W > 0$.

In Figure 8, we plot the decay rates $\rho(y)$ of the SINR and SIR distributions. The actual SINR is defined by $\mathring{\mathrm{SINR}} \triangleq \mathring{S}/(\mathring{I} + W)$, and the actual decay rate is accordingly. The noise is of the form $W = (d_0/\hat{d}_{h,\epsilon})^{\gamma}$. Also, we plot the decay rates of $\mathring{\mathrm{SIR}}$ and $\mathring{\mathrm{SINR}}$ with Nakagami-2 fading variables, *i.e.*, $\sqrt{g_x} \sim$ Nakagami$(2, 1)$ for all $x \in \Theta$ and with the LOS, when no fading is present. Notably, the tail of the SIR is similar in all fading settings. In the LOS case with noise, because $P = 1$, the SINR is at most 0 dB and, therefore, $\rho(y) = \infty$ for $y > 1$. The error in theory is due to the low elevation angle $\epsilon = 45°$, which causes a difference in the geometry. Also, κ does not correspond accurately to the mean number of UEs inside the 3 dB footprint with low elevation angles.

In Figure 9, we plot the theoretical SINR distribution and the simulated actual distribution for various κ and W. Contrary to the SIR distribution, smaller κ do not necessarily produce better coverage probabilities: With small densities, the served UE is likely to be far away from the SBS, and because of the path loss, the noise at the SBS's receiver will restrict the SINR.

Figure 10 plots the theoretical and the simulated actual expected SINR and SIR for various κ and W. The observed maximizing densities are approximately $\kappa_E^{[W]} \in \{0.5, 0.9, 1.2\}$ for $W \in \{0.3, 1, 3\} \cdot (d_0/\hat{d}_{h,\epsilon})^{\gamma}$, respectively. The expected SIR is an upper bound for the expected SINR for $\kappa > \log(2)$, and there is no upper bound if $\kappa \leq \log(2)$. To demonstrate that the theory describes the expected SIR and SINR in a generalized fading setting, we also plot the simulated values for Nakagami-2 fading and LOS.

In Figure 11, we plot the theoretical coverage probabilities with $\theta = 1$ and the actual coverage probabilities $\mathbb{P}(\mathring{\mathrm{SINR}} > \theta)$ and $\mathbb{P}(\mathring{\mathrm{SIR}} > \theta)$ for various κ and W. We also plot the coverage probabilities for the LOS and Nakagami-2 fading settings. The observed maximizing densities are given approximately by $\kappa_P^{[W,\theta]} \in \{0.7, 0.5, 0.4\}$ for $W \in \{1, 0.3, 0.01\} \cdot (d_0/\hat{d}_{h,\epsilon})^{\gamma}$, respectively. Comparing Figures 10 and 11, it can be seen that within roughly 50 percent difference marginal, $\kappa_E^{[W]} \approx \kappa_P^{[W,\theta]} \approx \log(2)$ for every W studied. However, this approximation of $\kappa_P^{[W,\theta]}$ cannot be accurate for general W because, for $W \to 0$, the SINR approaches the SIR and the maximizing $\kappa_P^{[W,\theta]} \to 0$. Similarly, $\kappa_E^{[W]}$ depends on W. If W is in the proximity of $(d_0/\hat{d}_{h,\epsilon})^{\gamma}$ (*i.e.*, the maximal SNR averaged over the fading is in the proximity of 0 dB; in Figures 10 and 11, between -20 dB and 4.8 dB), the maximizing κ is given roughly by $\log(2)$, which also is the threshold for the expected SIR being infinite.

Remark 2 (Power control)**.** If we denote with P_u the power of the served UE, it is easy to see that $F_{\mathrm{SINR}}(\theta)$ is derived from (34) by the scaling $\theta \mapsto \theta/P_u$. Therefore, the power control of the served UE scales the magnitude of $\mathbb{E}(\mathrm{SINR}_{\kappa,W})$ by a constant P_u. However, it does not affect the maximizing κ.

C. Throughput distribution

If we assume a Gaussian waveform for all transmissions, the normalized (Shannon) throughput, normalized bit rate, or the spectral efficiency of the communication channel without the noise is defined by $\tau_{\mathrm{SIR}}^{[\kappa]} \triangleq \log(1 + \mathrm{SIR}_{\kappa})/\log(2)$. The Laplace transform of the random variable $\tau_{\mathrm{SIR}}^{[\kappa]}$ is given in the positive half-plane of $\mathbb{C}$ by

$$\mathbb{E}(e^{-s\tau_{\mathrm{SIR}}^{[\kappa]}}) = \mathbb{E}(1 + \mathrm{SIR}_{\kappa})^{-s/\log(2)} = \frac{1}{\log(2)} \int_0^{\infty} \frac{F_{\mathrm{SIR}}^{[\kappa]}(v)}{1+v} dv = \frac{\kappa}{\kappa + s}, \qquad (42)$$

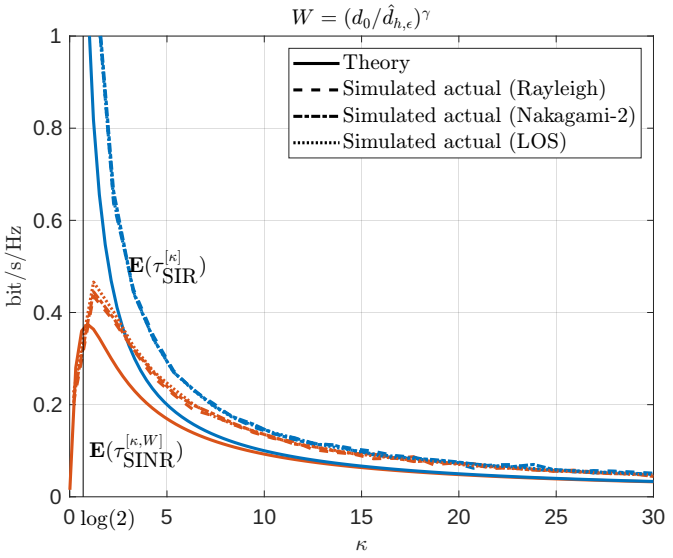

Fig. 12. The simulated actual and the theoretical expected throughput for $\kappa \in [0, 30]$ and $W = (d_0/\hat{d}_{h,\epsilon})^\gamma$. The parameters $\gamma = 4$, $h = 1200$ km, $\epsilon = 45°$, $\varphi_{\text{RX}} = 1.6$ and $\lambda \in [0, 2.1 \cdot 10^{-3}]/\text{km}^2$ were used to match the respective κ.

which is the Laplace transform of the exponential distribution with mean

$$\mathbb{E}(\tau_{\text{SIR}}^{[\kappa]}) = 1/\kappa. \tag{43}$$

Similarly, with the noise component, the expectation of $\tau_{\text{SINR}}^{[\kappa,W]} \triangleq \log(1 + \text{SINR}_{\kappa,W})/\log(2)$ is given by

$$\begin{aligned}\mathbb{E}(\tau_{\text{SINR}}^{[\kappa,W]}) &= \frac{1}{\log(2)} \int_0^\infty \frac{F_{\text{SINR}}^{[\kappa,W]}(v)}{1+v} dv \\ &= \frac{\tilde{\kappa}}{\log(2)} \int_0^\infty (1+v)^{-\tilde{\kappa}-1} E_{\tilde{\kappa}+1}\left(W(\hat{d}_{h,\epsilon}/d_0)^\gamma v\right) dv. \end{aligned} \tag{44}$$

The exact expression for (44) is complicated. However (the proof is given in Appendix D),

$$\mathbb{E}(\tau_{\text{SINR}}^{[\kappa,W]}) \sim 1/\kappa, \text{ as } \kappa \to \infty. \tag{45}$$

As for the expected SINR and the coverage probability, a maximizing $\kappa_T^{[W]} \triangleq \arg\max\{\kappa : \mathbb{E}(\tau_{\text{SINR}}^{[\kappa,W]})\}$ exists. In Figure 12, we plot the expected throughput for various κ and compare the theoretical $\mathbb{E}(\tau_{\text{SIR}}^{[\kappa]})$ and $\mathbb{E}(\tau_{\text{SINR}}^{[\kappa,W]})$ to the simulated $\mathbb{E}\log(1+\mathring{\text{SIR}})$ and $\mathbb{E}\log(1+\mathring{\text{SINR}})$, respectively. We also plot the simulated values in Nakagami-2 fading and the LOS cases. All fading cases are almost identical. The error in the theory is because of the small elevation angle $\epsilon = 45°$ that causes a significant difference in the geometry and because κ does not correspond accurately to the mean number of UEs inside the 3 dB footprint. Again, the optimal $\kappa_T^{[W]} \approx \log(2)$.

V. Conclusions

We presented a novel approximate system model for a low earth orbit (LEO) uplink. The model is accurate for high elevation angles and low altitudes. We introduced the gain process (GP), a heterogeneous Poisson point process (PPP) consisting of the approximate signal gains of the user equipments (UEs) inside the typical satellite base station's (SBS's) Gaussian antenna pattern. The relative gain process (RGP), which consists of the gains relative to the served UE, was shown to be equivalent to the GP. This point process follows by modeling the UEs on the two-dimensional plane, significantly simplifying the analysis compared to working with a point process on a sphere. We derived analytical expressions, some in closed form, for various performance metrics. The analysis matches the Monte Carlo simulated spherical system model. We derived the SIR, SINR, throughput distributions, and the SIR meta distribution (MD). We used an exponential power fading gain, *i.e.*, Rayleigh fading, in the analysis. However, quantitatively, the results apply to Nakagami-2 fading and the LOS for the tail distribution of the SIR, as well as for the first moments of the SIR, the SINR and the throughput. Qualitative insights go even further.

We showed that the critical parameter affecting the performance metrics is the mean number of co-channel UEs inside the SBS's 3 dB footprint; κ. For the SIR MD, we obtained closed-form expressions for the first two moments. Furthermore, we derived two analytical expressions for general complex and integer moments. The beta distribution can reliably approximate the SIR MD by matching the first two moments. We observed that the variance in the reliability of a SBS is highly dependent on the density of the UEs; to maintain a consistent user experience, we have to make the network dense. The distribution of SIR is a heavy-tailed Lomax distribution, but the SINR distribution has a thinner tail. With the noise, we found a density for which the expected SINR, coverage probability and throughput are maximized. In the interference-limited channel, the inverse of the mean number of UEs within the 3 dB footprint gives the expected spectral efficiency measured in bits. For small user densities ($\kappa < \log(2)$), the channel is essentially noise-limited, and one has to carefully address how the noise affects the performance (the interference energy component from the sidelobes can also be incorporated into the noise power constant because of its relatively small variance).

As a mathematical curiosity, the asymptotics of the expected SINR and the expected throughput revealed exciting asymptotical behavior of the exponential integral summarized in (57). In addition, an interesting representation of the generalized hypergeometric function was derived in (62).

The presented framework can be extended to other point processes. For example, one natural extension would be to randomize the elevation angle or the altitude of the SBS, leading to a random density parameter of the RGP and a Cox process. The presented framework may be helpful in other aerial base station (ABS) models in addition to the LEO setting. It would also be interesting to extend the analysis to other fading distributions. Because of the planar formulation of the analysis, one may directly exploit many results for two-dimensional stochastic geometry models of wireless networks. The quantitative and qualitative results enhance the understanding of dense LEO networks and hold mathematical importance in studying wireless networks using stochastic geometry.

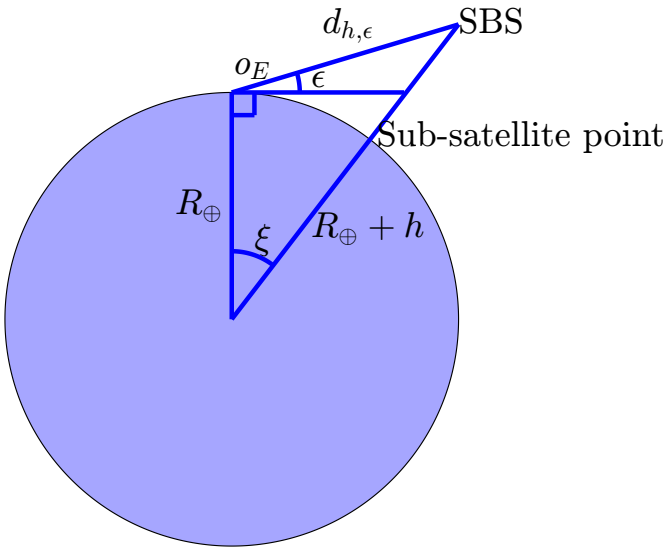

Fig. 13. Sketch of the geometry of the spherical model

APPENDIX A
GEOMETRY OF THE SPHERICAL SYSTEM MODEL

Directly from the law of cosines, we have

$$d_{h,\epsilon} = d_{h,\epsilon}(\xi) = \sqrt{R_\oplus^2 + (R_\oplus + h)^2 - 2R_\oplus(R_\oplus + h)\cos(\xi)}. \quad (46)$$

Furthermore, we may derive the relation between ϵ and ξ: The law of cosines states that

$$(R_\oplus + h)^2 = d_{h,\epsilon}(\xi)^2 + R_\oplus^2 - 2d_{h,\epsilon}(\xi)R_\oplus\cos(\pi/2 + \epsilon), \quad (47)$$

which is analytically solvable for ξ.

APPENDIX B
PROOF OF LEMMA 1

First, we derive the density function $\lambda_{\mathcal{G}}(\cdot)$ for the RGP, and after that, we will show that the RGP is a PPP.

For a PPP $\Phi = \{x_k\}_{k=1}^\infty$ of intensity λ on the plane, we consider that the interferer distances $\{\|x_k\|\}_{k=1}^\infty$ are ordered according to their distances to the origin. It follows that

$$\begin{aligned}
&\mathbb{P}(G[D_{h,\epsilon}\|x_k\|]/G[D_{h,\epsilon}\|x_0\|] \le r) \\
&= \mathbb{P}(2^{-((D_{h,\epsilon}\|x_k\|)^2 - (D_{h,\epsilon}\|x_0\|)^2)/\varphi_{\text{RX}}^2} \le r) \\
&= \mathbb{P}(-((D_{h,\epsilon}\|x_k\|)^2 - (D_{h,\epsilon}\|x_0\|)^2)/\varphi_{\text{RX}}^2 \le \log_2(r)) \\
&= \mathbb{P}(\|x_k\|^2 - \|x_0\|^2 \ge -\varphi_{\text{RX}}^2\log_2(r)/D_{h,\epsilon}^2,
\end{aligned}$$

where $D_{h,\epsilon}$ is given in (2). We define $y_k \triangleq \|x_k\|^2 - \|x_0\|^2$. The distances $\{y_k\}_{k=1}^\infty$ are Poisson distributed on $[0,\infty)$ with density $\pi\lambda$, and the distance y_k is Erlang distributed with parameters k and $\pi\lambda$, *i.e.*,

$$\begin{aligned}
&\mathbb{P}(y_k \ge -\varphi_{\text{RX}}^2\log_2(r)/D_{h,\epsilon}^2) \\
&= 1 - \frac{\gamma(k, -\pi\lambda\varphi_{\text{RX}}^2\log_2(r)/D_{h,\epsilon}^2)}{(k-1)!}.
\end{aligned}$$

The corresponding density is

$$-\frac{r^{-1+\frac{\pi\lambda\varphi_{\text{RX}}^2}{D_{h,\epsilon}^2\log(2)}}}{\log(r)}\left(\frac{-\pi\lambda\varphi_{\text{RX}}^2\log(r)}{D_{h,\epsilon}^2\log(2)}\right)^k/(k-1)!,$$

and the density function follows as

$$\begin{aligned}
\lambda_{\mathcal{G}}(r) &= -\frac{r^{-1+\frac{\pi\lambda\varphi_{\text{RX}}^2}{D_{h,\epsilon}^2\log(2)}}}{\log(r)}\sum_{k=1}^\infty\left(\frac{-\pi\lambda\varphi_{\text{RX}}^2\log(r)}{D_{h,\epsilon}^2\log(2)}\right)^k/(k-1)! \\
&\overset{(a)}{=} -\frac{r^{-1+\frac{\pi\lambda\varphi_{\text{RX}}^2}{D_{h,\epsilon}^2\log(2)}}}{\log(r)}\frac{-\pi\lambda\varphi_{\text{RX}}^2 r^{-\frac{\pi\lambda\varphi_{\text{RX}}^2}{D_{h,\epsilon}^2\log(2)}}\log(r)}{D_{h,\epsilon}^2\log(2)} \\
&= \frac{\pi\lambda\varphi_{\text{RX}}^2}{D_{h,\epsilon}^2\log(2)}r^{-1} = \tilde{\kappa}r^{-1},
\end{aligned}$$

where (a) follows from the identity $x\sum_{k=1}^\infty x^{k-1}/(k-1)! \equiv xe^x$. For small φ_{RX}, the term $\kappa = \pi\lambda\varphi_{\text{RX}}^2/D_{h,\epsilon}^2 = \pi\lambda\varphi_{\text{RX}}^2/(\sin^4(\epsilon)/h^2)$ in the constant $\tilde{\kappa} = \kappa/\log(2)$ is approximately the mean number of transmitters inside the 3 dB footprint, which can be seen by using the equation (2) and evaluating $\mathbb{E}\sum_{x\in\Phi}\mathbb{1}(\varphi_x < \varphi_{\text{RX}}) \approx \kappa = \mathbb{E}\sum_{x\in\Phi}\mathbb{1}(||x|| < h\varphi_{\text{RX}}/\sin^2(\epsilon)) = 2\lambda\pi\int_0^{h\varphi_{\text{RX}}/\sin^2(\epsilon)} rdr$, where $\mathbb{1}(\cdot)$ is the indicator function.

Next, we will derive the void probability of the RGP to show that it is a PPP. The cumulative density function (CDF) of the largest-gain is given by

$$\begin{aligned}
&\mathbb{P}(G[D_{h,\epsilon}\|x_0\|] \le r) = \mathbb{P}(2^{-D_{h,\epsilon}^2\|x_0\|^2/\varphi_{\text{RX}}^2} \le r) \\
&\le \mathbb{P}(\|x_0\|^2 \ge -\log_2(r)h^2\varphi^2/D_{h,\epsilon}^2) \\
&= r^{\pi\lambda\varphi_{\text{RX}}^2/(D_{h,\epsilon}\log(2))} = r^{\tilde{\kappa}}. \quad (48)
\end{aligned}$$

Let $\Phi_1 = \{\|x\|^2\}_{x\in\Phi}$. The void probability $\mathbb{P}[\mathcal{G}((a,b)) = 0]$ is given by

$$\begin{aligned}
&\mathbb{E}_R\mathbb{P}[(\mathcal{G}|(G[D_{h,\epsilon}\|x_0\|] = R))((a,b)) = 0] \\
&= \mathbb{E}_R\mathbb{P}[(\mathcal{G}|(2^{-((D_{h,\epsilon}\|x_0\|)^2/\varphi_{\text{RX}}^2)} = R))((a,b)) = 0] \\
&= \mathbb{E}_R\mathbb{P}\left[\Phi_1\left(\left(-\frac{\log(bR)\varphi_{\text{RX}}^2}{D_{h,\epsilon}\log(2)}, -\frac{\log(aR)\varphi_{\text{RX}}^2}{D_{h,\epsilon}\log(2)}\right)\right) = 0\right] \\
&\overset{(a)}{=} \int_0^1 \tilde{\kappa}r^{\tilde{\kappa}-1} \\
&\quad\cdot\mathbb{P}\left[\Phi_1\left(\left(-\frac{\log(br)\varphi_{\text{RX}}^2}{D_{h,\epsilon}\log(2)}, -\frac{\log(ar)\varphi_{\text{RX}}^2}{D_{h,\epsilon}\log(2)}\right)\right) = 0\right]dr \\
&= \int_0^1 \tilde{\kappa}r^{\tilde{\kappa}-1}e^{\tilde{\kappa}(\log(ar)-\log(br))}dr \\
&= \int_0^1 \tilde{\kappa}r^{\tilde{\kappa}-1}(a/b)^{\tilde{\kappa}}dr \\
&= (a/b)^{\tilde{\kappa}}. \quad (49)
\end{aligned}$$

In (a), we de-conditioned on R by using the probability density function (PDF) of the largest gain process derived from the CDF (48).

Further,

$$\exp\left\{-\int_a^b \lambda_{\mathcal{G}}(r)dr\right\} = \exp\left\{-\int_a^b \tilde{\kappa}/rdr\right\} = (a/b)^{\tilde{\kappa}}, \quad (50)$$

hence by Rényi's theorem $\mathcal{G}$ is Poisson [23, Thm. 2.24].

APPENDIX C
INVERSE LARGEST GAIN PROCESS

Using the CCDF of the largest gain (48), the CCDF of the inverse largest gain process is given by

$$F(r) = \mathbb{E}(1/G[D_{h,\epsilon}\|x_0\|] \geq r) = 1 - (1/r)^{\tilde{\kappa}}. \tag{51}$$

Let $u = 1/r$. By the chain rule, the PDF is given by

$$f(r) = F'(r) = \frac{du^C}{du}\frac{du}{dr} = C\left(\frac{1}{r}\right)^{\tilde{\kappa}-1} r^{-2} = \frac{\tilde{\kappa}}{r^{1+\tilde{\kappa}}},$$

and the Laplace transform of the inverse largest gain is given directly in terms of the exponential integral

$$\begin{aligned}&\mathbb{E}(e^{-s/G[D_{h,\epsilon}\|x_0\|]})\\ &= \int_1^\infty f(r)e^{-rs}dr = \tilde{\kappa}\int_1^\infty \frac{e^{-rs}}{r^{1+\tilde{\kappa}}}dr\\ &= \tilde{\kappa}E_{\tilde{\kappa}+1}(s).\end{aligned} \tag{52}$$

APPENDIX D
ASYMPTOTIC BEHAVIOR OF $\mathbb{E}(\text{SINR}_{\kappa,W})$ AND $\tau_{\text{SINR}}^{[\kappa,W]}$

All mass of the largest-gain distribution (48) is concentrated at $r = 1$ when $\kappa \to \infty$. Hence, by Corollary 1, the Laplace transform of the sum $X \equiv \sum_{x\in\Phi\setminus\{x_0\}} G[D_{h,\epsilon}\|x\|]$ in the limit $\kappa \to \infty$ is given by substituting $v = e^{-sr}, s > 0$, to 19. Furthermore, we may take a first-order Taylor expansion of the exponent of the Laplace transform at $s = 0$, which yields

$$\mathcal{L}_X(s) \sim e^{-\tilde{\kappa}s}, \text{ as } s \to 0. \tag{53}$$

When $\kappa \to \infty$, the tail of (53) goes to 0. Hence, for the first negative moment it holds that [30, Eq. 1]

$$\begin{aligned}\mathbb{E}\left(1/X\right) &= \int_0^\infty \mathcal{L}_X(s)ds\\ &\sim \int_0^\infty e^{-\tilde{\kappa}s}ds = 1/\tilde{\kappa} \text{ as } \kappa \to \infty.\end{aligned} \tag{54}$$

Consequently,

$$\begin{aligned}1 &\leq \frac{\mathbb{E}(\text{SIR}_\kappa)}{\mathbb{E}(\text{SINR}_{\kappa,W})} = \frac{\mathbb{E}(S/I)}{\mathbb{E}(S/(I+W))}\\ &= \frac{\mathbb{E}\left(1/X\right)}{\mathbb{E}(1/(X + W(\hat{d}_{h,\epsilon}/d_0)^\gamma))}\\ &\overset{(a)}{\leq} \frac{\mathbb{E}\left(1/X\right)}{1/(\mathbb{E}\left(X\right) + W(\hat{d}_{h,\epsilon}/d_0)^\gamma)}\\ &= \mathbb{E}\left(1/X\right)\mathbb{E}\left(X\right) + \mathbb{E}\left(1/X\right)W(\hat{d}_{h,\epsilon}/d_0)^\gamma\\ &\overset{(b)}{=} 1/\tilde{\kappa}\cdot\tilde{\kappa} + 1/\tilde{\kappa}\cdot W(\hat{d}_{h,\epsilon}/d_0)^\gamma = 1, \text{ as } \kappa \to \infty,\end{aligned} \tag{55}$$

i.e., $\mathbb{E}(\text{SINR}_{\kappa,W}) \sim \mathbb{E}(\text{SIR}_\kappa) = 1/(\tilde{\kappa}-1)$, as $\kappa \to \infty$. In (a), we use Jensen's inequality, and in (b) we use (54), and $\mathbb{E}(X)$ is derived as in (10).

Furthermore,

$$\begin{aligned}1 &\leq \frac{\mathbb{E}(\tau_{\text{SIR}}^{[\kappa]})}{\mathbb{E}(\tau_{\text{SINR}}^{[\kappa,W]})} = \frac{\mathbb{E}\log(1+\text{SIR}_\kappa)}{\mathbb{E}\log(1+\text{SINR}_{\kappa,W})}\\ &\overset{(c)}{\leq} \frac{\mathbb{E}(\text{SIR}_\kappa)}{\mathbb{E}(\text{SINR}_{\kappa,W})/(\mathbb{E}(\text{SINR}_{\kappa,W})+1)}\\ &= \frac{\mathbb{E}(\text{SIR}_\kappa)}{\mathbb{E}(\text{SINR}_{\kappa,W})}(\mathbb{E}(\text{SINR}_{\kappa,W})+1) = 1,\end{aligned} \tag{56}$$

i.e., $\mathbb{E}(\tau_{\text{SINR}}^{[\kappa,W]}) \sim \mathbb{E}(\tau_{\text{SIR}}^{[\kappa]}) = 1/\kappa$, as $\kappa \to \infty$. In (c), we exploit the inequality $\log(1+x) > x/(x+1)$ and Jensen's inequality.

Write out the asymptotic limits according to (36) and (44), then for any $c \triangleq W(\hat{d}/d_0)^\gamma > 0$

$$\begin{cases}\tilde{\kappa}\displaystyle\int_0^\infty (1+y)^{-\tilde{\kappa}}E_{\tilde{\kappa}+1}\left(cy\right)dy \sim \frac{1}{\tilde{\kappa}-1},\\ \tilde{\kappa}\displaystyle\int_0^\infty (1+y)^{-\tilde{\kappa}-1}E_{\tilde{\kappa}+1}\left(cy\right)dy \sim \frac{1}{\tilde{\kappa}},\end{cases} \tag{57}$$

as $\tilde{\kappa} \to \infty$.

APPENDIX E
MOMENTS OF THE SIR MD

We have

$$\begin{aligned}\mathcal{P}(\theta) &= \mathbb{P}\left(g_{x_0} > \theta \sum_{x\in\Phi\setminus\{x_0\}} \frac{G[D_{h,\epsilon}\|x\|]}{G[D_{h,\epsilon}\|x_0\|]}g_x\Big|\Phi\right)\\ &= \prod_{x\in\Phi\setminus\{x_0\}} \frac{1}{1+\theta\frac{G[D_{h,\epsilon}\|x\|]}{G[D_{h,\epsilon}\|x_0\|]}} = \prod_{x\in\mathcal{G}} \frac{1}{1+\theta x}.\end{aligned}$$

The bth moment follows as

$$M_b(\theta) = \mathbb{E}\prod_{x\in\mathcal{G}} \frac{1}{(1+\theta x)^b}.$$

Using the PGFL (19) of the RGP for $v(x) = 1/(1+\theta x)^b$;

$$M_b(\theta) = \exp\left\{-\tilde{\kappa}\int_0^1 \left(1 - \frac{1}{(1+\theta r)^b}\right)/r dr\right\}. \tag{58}$$

For $b = 1$, the integral has the value

$$\begin{aligned}&= \int_0^1 \left(1 - \frac{1}{1+\theta r}\right)/r dr\\ &= \int_0^1 \frac{\theta}{1+\theta r}dr = \int_1^{1+\theta} \frac{1}{u}du = \log(1+\theta).\end{aligned} \tag{59}$$

For $b = 2$,

$$\begin{aligned}&\int_0^1 \left(1 - \frac{1}{(1+\theta r)^2}\right)/r dr\\ &= \int_0^1 \left(\frac{2\theta}{(1+\theta r)^2} + \frac{\theta^2 r}{(1+\theta r)^2}\right)dr\\ &\overset{(a)}{=} \int_0^1 \left(\frac{2\theta}{(1+\theta r)^2} - \frac{\theta}{(1+\theta r)^2} + \frac{\theta^2}{\theta+\theta^2 r}\right)dr\\ &= \int_1^{1+\theta} \frac{1}{u^2}du + v\int_\theta^{\theta+\theta^2} \frac{1}{v}dv = \frac{\theta}{1+\theta} + \log(1+\theta).\end{aligned} \tag{60}$$

In (a), we used the partial fraction expansion for the latter term in the integrand.

For $b \in \mathbb{C}$, the integral can be expressed with the generalized hypergeometric function

$$\int_0^1 \left(1 - \frac{1}{(1+\theta r)^b}\right)/r dr = \theta b\,{}_3F_2(1,1,1+b;2,2;-\theta). \tag{61}$$

Using the definition of the hypergeometric series, for $|\theta| < 1$ and $b \in \mathbb{N}$;

$$
\begin{aligned}
&{}_3F_2(1,1,1+b;2,2;-\theta) = \sum_{n=0}^{\infty} \frac{(1)_n (1)_n (1+b)_n}{(2)_n (2)_n} \frac{(-\theta)^n}{n!} \\
&= \sum_{n=0}^{\infty} \frac{(1+b)_n}{(n+1)^2 n!} (-\theta)^n = \frac{1}{b!} \sum_{n=0}^{\infty} \frac{(n+1)_b}{(n+1)^2} (-\theta)^n \\
&\overset{(a)}{=} \frac{1}{b!} \sum_{n=0}^{\infty} \frac{\sum_{k=1}^{b} \left[{b \atop k} \right] (n+1)^k}{(n+1)^2} (-\theta)^n \\
&= \frac{1}{b!} \sum_{k=1}^{b} \left[{b \atop k} \right] \sum_{n=0}^{\infty} \frac{(-\theta)^n}{(n+1)^{2-k}} \overset{(b)}{=} -\frac{1}{b!} \sum_{k=1}^{b} \left[{b \atop k} \right] \frac{\mathrm{Li}_{2-k}(-\theta)}{\theta}.
\end{aligned}
\tag{62}
$$

In (a), we used the expansion of the rising Pochhammer factorial; in (b) we used the definition of the polylogarithm. Furthermore, the polylogarithm can be extended to $|\theta| \geq 1$ by analytic continuation. In particular, for $\theta > 0$, we have $\mathrm{Li}_1(-\theta) = -\log(1+\theta)$. We acquire the order $2-k$ polylogarithm, *e.g.*, through the recursive relation $\mathrm{Li}_{s+1}(-\theta) = -\int_0^\theta \mathrm{Li}_s(-t)/t dt$, which shows that $\mathrm{Li}_{2-k}(-\theta)$ is well-defined for all $\theta > 0$.

REFERENCES

[1] B. Di, L. Song, Y. Li, and H. V. Poor, "Ultra-dense LEO: Integration of satellite access networks into 5G and beyond," *IEEE Wireless Communications*, vol. 26, no. 2, pp. 62–69, 2019.

[2] M. Höyhtyä, S. Boumard, A. Yastrebova, P. Järvensivu, M. Kiviranta, and A. Anttonen, "Sustainable satellite communications in the 6G era: A european view for multilayer systems and space safety," *IEEE Access*, vol. 10, pp. 99 973–100 005, 2022.

[3] M. Jia, X. Gu, Q. Guo, W. Xiang, and N. Zhang, "Broadband hybrid satellite-terrestrial communication systems based on cognitive radio toward 5G," *IEEE Wireless Communications*, vol. 23, no. 6, pp. 96–106, 2016.

[4] 3GPP, "Solutions for NR to support non-terrestrial networks (NTN), TR 38.821," 3GPP, Tech. Rep., 2023.

[5] R. Wang, M. A. Kishk, and M.-S. Alouini, "Ultra-dense LEO satellite-based communication systems: A novel modeling technique," *IEEE Communications Magazine*, vol. 60, no. 4, pp. 25–31, 2022.

[6] M. Haenggi, "Meta distributions—part 1: Definition and examples," *IEEE Communications Letters*, vol. 25, no. 7, pp. 2089–2093, 2021.

[7] ——, "The meta distribution of the SIR in Poisson bipolar and cellular networks," *IEEE Transactions on Wireless Communications*, vol. 15, no. 4, pp. 2577–2589, 2016.

[8] M. Matracia, M. A. Kishk, and M.-S. Alouini, "Aerial base stations for global connectivity: Is it a feasible and reliable solution?" *IEEE Vehicular Technology Magazine*, vol. 18, no. 4, pp. 94–101, 2023.

[9] H. Lin, C. Zhang, Y. Huang, R. Zhao, and L. Yang, "Fine-grained analysis on downlink LEO satellite-terrestrial mmwave relay networks," *IEEE Wireless Communications Letters*, vol. 10, no. 9, pp. 1871–1875, 2021.

[10] Y. Sun and Z. Ding, "A fine grained stochastic geometry-based analysis on LEO satellite communication systems," *IEEE Networking Letters*, vol. 5, no. 4, pp. 237–240, 2023.

[11] A. Yastrebova, I. Angervuori, N. Okati, M. Vehkaperä, M. Höyhtyä, R. Wichman, and T. Riihonen, "Theoretical and simulation-based analysis of terrestrial interference to LEO satellite uplinks," in *GLOBECOM 2020 - 2020 IEEE Global Communications Conference*, 2020, pp. 1–6.

[12] N. Okati and T. Riihonen, "Downlink and uplink low earth orbit satellite backhaul for airborne networks," in *2022 IEEE International Conference on Communications Workshops (ICC Workshops)*, 2022, pp. 550–555.

[13] H. Jia, C. Jiang, L. Kuang, and J. Lu, "An analytic approach for modeling uplink performance of mega constellations," *IEEE Transactions on Vehicular Technology*, vol. 72, no. 2, pp. 2258–2268, 2023.

[14] X. Hu, B. Lin, P. Wang, X. Lu, H. Wei, and S. Qi, "Modeling and analysis of end-to-end LEO satellite-aided shore-to-ship communications," in *2023 IEEE/CIC International Conference on Communications in China (ICCC)*, 2023, pp. 1–6.

[15] H. Jia, Z. Ni, C. Jiang, L. Kuang, and J. Lu, "Uplink interference and performance analysis for megasatellite constellation," *IEEE Internet of Things Journal*, vol. 9, no. 6, pp. 4318–4329, 2022.

[16] C. C. Chan, B. Al Homssi, and A. Al-Hourani, "A stochastic geometry approach for analyzing uplink performance for IoT-over-satellite," in *ICC 2022 - IEEE International Conference on Communications*, 2022, pp. 2363–2368.

[17] B. Al Homssi and A. Al-Hourani, "Optimal beamwidth and altitude for maximal uplink coverage in satellite networks," *IEEE Wireless Communications Letters*, vol. 11, no. 4, pp. 771–775, 2022.

[18] B. A. Homssi and A. Al-Hourani, "Modeling uplink coverage performance in hybrid satellite-terrestrial networks," *IEEE Communications Letters*, vol. 25, no. 10, pp. 3239–3243, 2021.

[19] C. Li, Z. Fang, Y. Wang, and C. Sun, "An approach for interference modeling and analysis of low orbit satellite internet," in *2023 IEEE 23rd International Conference on Communication Technology (ICCT)*, 2023, pp. 1178–1184.

[20] I. Angervuori and R. Wichman, "A closed-form approximation of the SIR distribution in a LEO uplink channel," in *2022 IEEE Globecom Workshops (GC Wkshps): Workshop on Cellular UAV and Satellite Communications, December 4 - 8, Rio de Janeiro, Brazil*, 2022.

[21] X. Wang and M. Haenggi, "The Chebyshev-Markov inequalities," University of Notre Dame, Tech. Rep., 2022. [Online]. Available: https://www3.nd.edu/~mhaenggi/pubs/techreport_cm22.pdf

[22] I. T. U. Recommendation, "Satellite antenna radiation patterns for non-geostationary orbit satellite antennas operating in the fixed-satellite service below 30 GHz," International Telecommunications Union, Tech. Rep. Rec. ITU-R S.1528, 2001. [Online]. Available: https://www.itu.int/dms_pubrec/itu-r/rec/s/R-REC-S.1528-0-200106-I!!PDF-E.pdf

[23] M. Haenggi, *Stochastic geometry for wireless networks*. Cambridge: Cambridge University Press,, 2013.

[24] M. Albulet, "SpaceX V-band non-geostationary satellite system," Space Exploration Technologies Corp., Tech. Rep., 2017.

[25] B. Błaszczyszyn, M. Haenggi, P. Keeler, and S. Mukherjee, *Stochastic Geometry Analysis of Cellular Networks*. Cambridge University Press, 2018.

[26] Y. Wang, M. Haenggi, and Z. Tan, "The meta distribution of the SIR for cellular networks with power control," *IEEE Transactions on Communications*, vol. 66, no. 4, pp. 1745–1757, 2018.

[27] ——, "SIR meta distribution of k -tier downlink heterogeneous cellular networks with cell range expansion," *IEEE Transactions on Communications*, vol. 67, no. 4, pp. 3069–3081, 2019.

[28] K. Gulati, B. L. Evans, J. G. Andrews, and K. R. Tinsley, "Statistics of co-channel interference in a field of Poisson and Poisson-Poisson clustered interferers," *IEEE Transactions on Signal Processing*, vol. 58, no. 12, pp. 6207–6222, 2010.

[29] S. Foss, D. Korshunov, and S. Zachary, *An Introduction to Heavy-Tailed and Subexponential Distributions*, 2nd ed., ser. Springer Series in Operations Research and Financial Engineering. New York, NY: Springer Nature, 2013.

[30] N. Cressie, A. S. Davis, J. L. Folks, and G. E. P. II, "The moment-generating function and negative integer moments," *The American Statistician*, vol. 35, no. 3, p. 148, 1981.